Icarus 311 (2018) 242–257

Contents lists available at ScienceDirect

Icarus

journal homepage: www.elsevier.com/locate/icarus

A global database and statistical analyses of (4) Vesta craters

Zhaoqin Liu[a], Zongyu Yue[a,*], Gregory Michael[b], Sheng Gou[a,c], Kaichang Di[a,c], Shujuan Sun[d], Jianzhong Liu[e]

[a] State Key Laboratory of Remote Sensing Science, Institute of Remote Sensing and Digital Earth, Chinese Academy of Sciences, Beijing 100101, China
[b] Institute of Geological Sciences, Freie Unversitaet Berlin, Malteser Strasse 74-100, Haus D, Berlin 12249, Germany
[c] Lunar and Planetary Science Laboratory, MUST – Partner Laboratory of Key Laboratory of Lunar and Deep Space Exploration, CAS, Macau, China
[d] Sichuan Remote Sensing Geoinformatics Institute, Chengdu 610100, China
[e] Institute of Geochemistry Chinese Academy of Sciences, Guiyang 550002, China

ARTICLE INFO

Article history:
Received 29 November 2017
Revised 26 March 2018
Accepted 9 April 2018
Available online 12 April 2018

Keywords:
(4) Vesta
Crater database
Morphometric parameters

ABSTRACT

In this paper, we present a global database of craters larger than 0.7 km in diameter on the surface of (4) Vesta, which we created based on a global mosaic of the Dawn spacecraft's high-altitude mapping orbit (HAMO) images at a resolution of ~60 m/pixel and cross-checked using the images from the low-altitude mapping orbit (LAMO) mission phase. The method to produce the crater database consists of visual crater identification and mathematical shape determination. To give precise measurements, topographic corrections have also been considered by combining the digital elevation model (DEM) data in this global survey. We calculated the morphometric parameters of the craters, which consist of diameter, depth, depth-to-diameter ratio, ellipticity, and azimuth of the major axis. Our results show that the craters on (4) Vesta are very shallow, with a mean depth-to-diameter ratio of ~0.065, which is similar to that of the craters on (1) Ceres and (25143) Itokawa but lower than for craters on other solid bodies. The results also show that the fractions of craters with an ellipticity greater than 1.1 or 1.2 are smaller than those of craters on the Martian surface, which is probably because few secondaries exist on the surface of (4) Vesta. In addition, the azimuths of the major axis are almost uniformly distributed in different directions. Our globally consistent crater database has many potential applications for future studies such as geologic mapping and surface age dating.

1. Introduction

Asteroid (4) Vesta, the second most massive object in the asteroid main belt, is an ellipsoidal asteroid with estimated dimensions of $286.3 \times 278.6 \times 223.2 \pm 0.1$ km (Russell et al., 2012). It has long been a target of scientific interest and has been studied through ground-based telescopes (McCord et al., 1970) and the Hubble Space Telescope (e.g., Binzel et al., 1997; Li et al., 2010), because of its geologic diversity (e.g., Degewij et al., 1979; Binzel et al., 1997) and the discovery that Howardite, eucrite, and diogenite meteorites are very likely samples excavated from Vesta (e.g., McCord et al., 1970; Binzel and Xu, 1993). As an object that formed early and possibly a remnant of an intact protoplanet, it is also expected to provide important clues to the processes that take place in the earliest phase of solar system formation (Russell et al., 2004, 2012). It was the first target of the Dawn mission, which was launched on 27 September 2007 and successfully entered orbit around (4) Vesta on 16 July 2011 after nearly four years of interplanetary flight (Rayman and Mase, 2014). The Dawn spacecraft orbited the (4) Vesta for over one year to September 2012 and imaged the entire surface (Russell et al., 2012). Equipped with two identical framing cameras (FC) (Rayman et al., 2006; Rayman and Mase, 2014), the Dawn spacecraft mapped (4) Vesta from three different orbital heights: a 2700 km altitude during the survey orbit, 700 km altitude during high altitude mapping orbit (HAMO), and 210 km altitude during low altitude mapping orbit (LAMO) (Russell and Raymond, 2011) resulting in spatial resolutions of ~260 m/pixel, ~60 m/pixel, and ~20 m/pixel, respectively (Roatsch et al., 2013; Nathues et al., 2015). Because only ~80% of the surface of (4) Vesta was covered during the survey mission phase (Marchi et al., 2012) and 84% of the surface was covered during the LAMO mission phase (Roatsch et al., 2013), a global mosaic has been constructed from the images taken during the HAMO (Roatsch et al., 2012, 2013). In addition, the surface of (4) Vesta was imaged several times during the HAMO and LAMO phase under similar illumination conditions with different viewing angles, allowing the generation of stereo topographic maps (Preusker et al., 2014). These data sets are very important for the study of the surface properties of (4) Vesta, and have been used for geologic study both

* Corresponding author.
E-mail address: yuezy@radi.ac.cn (Z. Yue).

https://doi.org/10.1016/j.icarus.2018.04.006
0019-1035/

regionally (e.g., Willams et al., 2014; Yingst et al., 2014) and globally (e.g., Jaumann, 2012; Ruesch et al., 2014).

Impact craters were proposed to be the major landform on the surface of (4) Vesta even before the Dawn mission (Gaffey, 1997), and studies based on Dawn data further confirm that it is indeed dominated by impact craters at all scales (Marchi et al., 2012). Craters are very important in planetary studies, not only because the cratering itself can contribute to investigations of the properties of surface or subsurface materials (e.g., the dark materials on (4) Vesta are closely related with impact craters; McCord et al., 2012; Jaumann et al., 2014), but also because crater populations can provide valuable information for regional or global geologic studies, especially for bodies where in situ rock samples are lacking, such as (4) Vesta, and impact crater counts are the only way to estimate the age of geologic units (e.g., Shoemaker et al., 1962; Trask, 1966). For these reasons, crater databases for the Moon (e.g., Kinser et al., 2013; Robbins, 2016), Mercury (Fassett et al., 2011), and Mars (e.g., Barlow, 1988, 2003; Salamunićcar et al., 2011; Robbins and Hynek, 2012a) have been established. Marchi et al. (2012) mapped 1872 craters larger than 4 km in diameter on the surface of (4) Vesta based on the visual image mosaic during the survey mission phase, and Vincent et al. (2014) selectively mapped 1025 craters ranging from 1.5 to 64 km in diameter. In addition, Kneissl et al., (2011) mapped 2892 asymmetric craters ranging in diameter from 0.3 to 43 km. However, a global crater database including a variety of important attributes, such as the crater positions, diameters, depths, and morphologies, has not yet been developed. These attributes have a broad range of science applications. For example, the crater database of Mars created by Robbins and Hynek (2012a) includes up to 70 fields to comprehensively describe the above attributes of the Mars craters and has been widely used in the analysis of Martian resurfacing events (Irwin et al., 2013), geological unit dating (Platz et al., 2013), global geologic mapping (Tanaka et al., 2014), and other studies.

When developing a crater database, craters can be either manually identified (e.g., Fassett et al., 2011; Robbins and Hynek, 2012a; Robbins, 2016) or machine catalogued (e.g., Salamunićcar and Lončarić, 2008; Stepinski et al., 2009; Salamunićcar et al., 2011). Although manual crater identification and measurement techniques can usually generate results that are closer to ground truth, Salamunićcar et al. (2011) and Robbins et al. (2014) pointed out that manual assignment of the crater and diameter may vary even between successive determinations by the same human operator or different researchers. However, it is inevitable that some craters are omitted or falsely detected when computer detection algorithms are used alone (see the evaluations of the automated detection results in the above studies). Therefore, it is better to combine the advantages of both methods when developing a crater database, that is, to manually identify the craters initially and then adjust the location and diameter locally with a higher precision using a robust detection algorithm.

In this study, we focus on developing a reliable global crater database for (4) Vesta. First, the data sets used in the research are introduced (Section 2), and then the methodology to create the crater database is described in detail (Section 3). In particular, we elaborate on the fields used to describe the attributes of the craters, explain their implications and how they are measured or calculated, and statistically analyze their inherent uncertainties. Next, we present the results and analyses of the crater database, including the database completeness, global distribution, and morphometric parameters (Section 4). We also compare the craters in the new database with both the previously identified craters on 4) Vesta and craters on other bodies (Section 5). Finally, we summarize the data analysis results and some potential scientific applications (Section 6).

2. Data sets

The data sets used in this work were acquired from the 1024×1024-pixel charge-coupled device (CCD) sensor of FC2 during Dawn's two HAMO phases (HAMO-1 and HAMO-2) and LAMO phase (Polanskey et al., 2011; Rayman and Mase, 2014). Dawn completed the HAMO-1 science phase from 1 October 2011 to 3 December 2011, during which (4) Vesta was globally covered six times, yielding a rich set of images (Rayman and Mase, 2014). From 15 June 2012 to 25 July 2012, Dawn carried out its HAMO-2 science phase, which focused on the northern regions that were previously in darkness (Rayman and Mase, 2014). As a result, at least 95% of Vesta's surface was imaged under similar illumination conditions but different viewing conditions; this enabled the Dawn team to construct stereo topographic maps as well as ortho-image mosaics (Preusker et al., 2014). The Dawn LAMO phase was carried out from 12 December 2011 to 1 May 2012, during which FC2 imaged nearly the entire illuminated surface (Rayman and Mase, 2014). However, the LAMO mission phase occurred during northern winter when the north pole region was in darkness; only 84% of the surface was illuminated and good illumination for crater identification was only available for 66.8% of the surface (Roatsch et al., 2013).

The above raw images were calibrated and converted to radiometric units and ortho-rectified (Schröder et al., 2013, 2014), resulting in several mosaics (Ruesch et al., 2014). In this research, two global mosaics of the images acquired during the HAMO and LAMO phases (Roatsch et al., 2012, 2013) are used, and their resolutions are ~60 m/pixel and 20 m/pixel, respectively. In addition, to map the craters in regions poleward from 70° latitude, another two mosaics from the HAMO images in north and south polar stereographic projections are used. These data products can be directly downloaded from planetary data system website (https://sbn.psi.edu/pds/resource/dawn/dwnvfcL1.html). Note that the two mosaics with north and south polar stereographic projections were derived from those images with good illumination conditions in the polar regions for the identification of craters. The mosaics of the HAMO images were first used to identify craters, and the mosaic of the LAMO images was used to cross-check the results, where possible. The reason that the LAMO mosaic was not first used to map the craters is to keep the diameter measurements of the identified craters consistent. To calculate the depths of the craters, we used a DEM of (4) Vesta, which was derived using stereo photogrammetry (Preusker et al., 2014). The DTM covers approximately 95% of the Vestan surface, except for a few permanently shadowed areas near the poles, which were interpolated. It has a resolution of ~70 m/pixel with a vertical accuracy of ~±6 m (Preusker et al., 2014). All data can be downloaded from https://sbn.psi.edu/pds/resource/dwnvfc2.html.

3. Methodology

In this section, we first analyze the characteristics of the craters on the surface of (4) Vesta, which is important for selecting suitable fields for the crater database. We subsequently detail the crater identification and measurement methods. In terms of the measurement errors, a detailed description of the circle and ellipse fitting is described in Appendix A. The flowchart of the process is shown in Fig. 1, and the detailed processing steps are described in the corresponding sections.

3.1. Properties of (4) Vesta craters and selected fields in the database

Although all impact craters on a given planetary body can be simply described as circular rimmed depressions, detailed

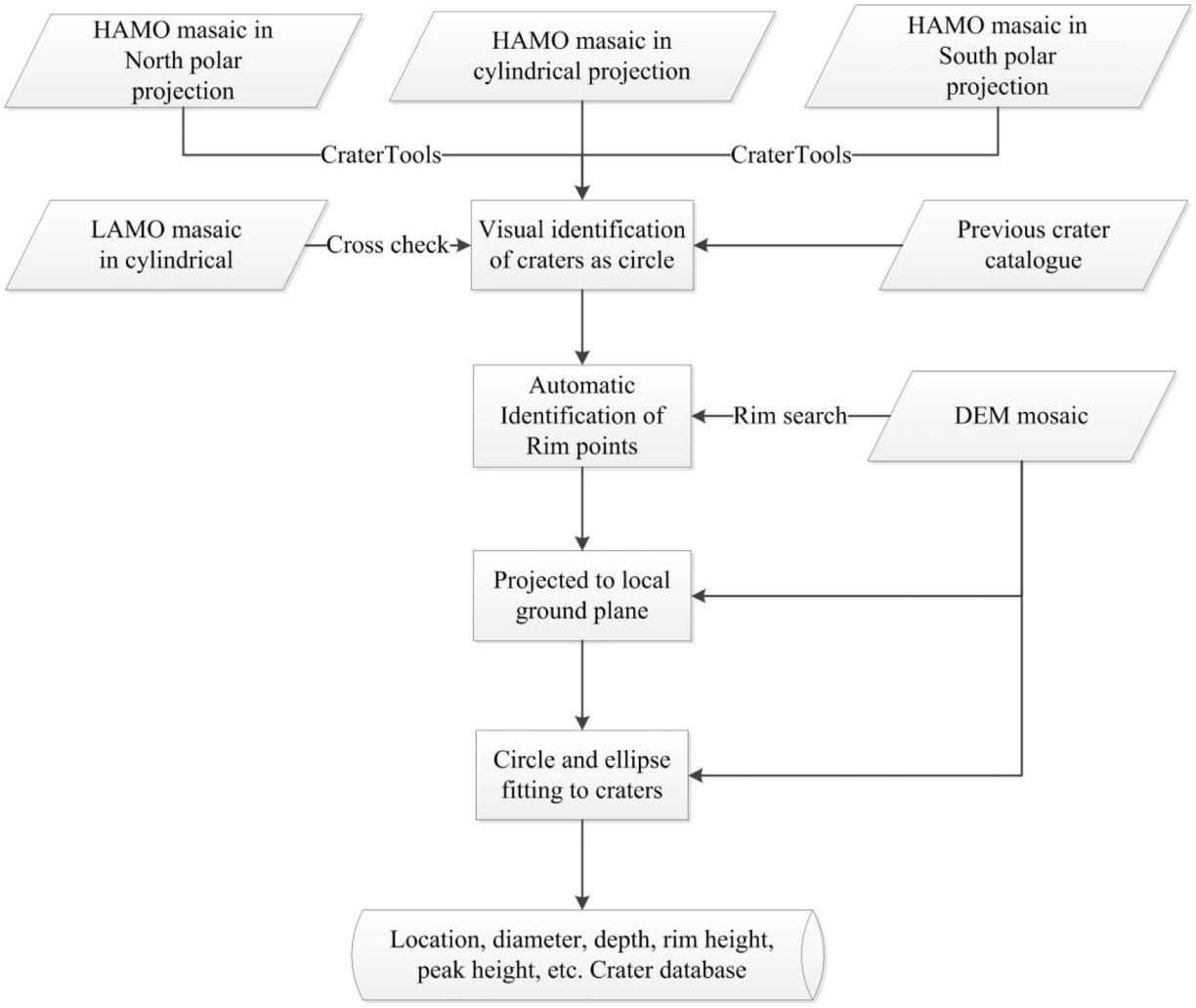

Fig. 1. Flowchart for the creation of the crater database for the surface of (4) Vesta.

crater morphology is a function of the diameter and preservation (Melosh, 1989). As the diameter increases, the morphology of craters usually ranges from bowl-shaped simple, complex with central peaks, complex with peak rings, to giant basins. Moreover, the transition diameters between the different morphologies are inversely proportional to the surface gravity (Melosh, 1989). Therefore, the transition diameter from simple to central-peak complex craters on (4) Vesta should be 73–147 km (this transition diameter on the Moon is 10–20 km, Pike, 1977a; Melosh, 1989). Further, the transition diameter from central peak-to-peak ring craters on (4) Vesta should be ~1032 km (this transition diameter on the Moon is ~140 km, Melosh, 1989). In agreement with expectations, only Vesta's largest crater, Rheasilvia, with a diameter of 500 ± 20 km (e.g., Jaumann, 2012; Salamunićcar and Lonćarić, 2008), has been reported to have a central peak (Salamunićcar and Lonćarić, 2008). Considering that studies have specifically investigated Rheasilvia (e.g., Ivanov and Melosh, 2013; Salamunićcar and Lonćarić, 2008), it is excluded in this research and only the simple craters are considered.

Although most craters appear circular in planform, for low angle impacts, the crater planform becomes elliptical with the major axis oriented with respect to the projectile's direction of travel (Herrick and Hessen, 2006). Impact on sloping surfaces also favored the formation of asymmetric craters as Kneissl et al., (2011) demonstrated. In addition, a recent numerical study of oblique impact also found that a lower impact velocity promotes the formation of elliptical craters (Elbeshausen et al., 2013). The mean impact velocity on the surface of (4) Vesta is ~4.75 km/s (Brien et al., 2011), which is less than that for the Moon (~17.4 km/s; Yue et al., 2013), where elliptical craters only make up ~5.4% of the total (Bottke et al., 2000). Thus, there should be a higher percentage of elliptical craters on the surface of (4) Vesta. In addition, the rugged target terrain also increases the percentage of elliptical craters, as Kneissl et al. (2011) demonstrated for (4) Vesta and Herrick et al. (2012) demonstrated in the Saturnian satellites (where 7.6% craters have ellipticities larger than 1.2); therefore, a higher percentage of elliptical craters on (4) Vesta is also expected considering the complex topography at all spatial scales (Jaumann, 2012). Hence, parameters to describe elliptical craters are included in the database.

Based on these properties of (4) Vesta craters and referring to previous crater databases (Li et al., 2010; Robbins and Hynek, 2012b; Wang et al., 2015), we selected 18 fields (columns) for the crater database of (4) Vesta (Table 1).

3.2. Crater identification and measurement

In this research, the craters were measured along the crater rim, i.e., the resultant diameter is the rim diameter (see Turtle et al., 2005), which is also often utilized in other crater databases (e.g., Robbins and Hynek, 2012a; Wang et al., 2015; Robbins, 2016). Three points along the crater rim were first identified in the

Table 1
Columns in the database and their brief descriptions. The capitalized text in the remainder of this section indicates the column names as they appear in the database.

Fields	Description
LONGITUDE_CIRCLE	Longitude from the derived center of a nonlinear least squares circle fit to the vertices in the DEM selected to identify the crater rim. Units: decimal degrees east.
LATITUDE_CIRCLE	Latitude from the derived center of a nonlinear least squares circle fit to the vertices in the DEM selected to identify the crater rim. Units: decimal degrees north.
ERROR_LONGITUDE_CIRCLE	Longitudinal errors from the circle fitting
ERROR_LATITUDE_CIRCLE	Latitudinal errors from the circle fitting.
DIAM_CIRCLE	Diameter of a nonlinear least squares circle fit to the vertices in the DEM selected to identify the crater rim. Units: km.
ERROR_DIAM_CIRCLE	Errors in the diameter from the circle fitting.
PTS_USED_CIRCLE	Number of points selected around the crater rim to fit the crater with a circle.
RMS_CIRCLE_FIT	RMS of fitting the crater with a circle. Units: m.
LONGITUDE_ELLIPSE	Longitude from the derived center of a nonlinear least squares ellipse fit to the vertices in the DEM selected to identify the crater rim. Units: decimal degrees east.
ERROR_LONGITUDE_ELLIPSE	Longitudinal errors from the ellipse fitting.
LATITUDE_ELLIPSE	Latitude from the derived center of a nonlinear least squares ellipse fit to the vertices in the DEM selected to identify the crater rim. Units: decimal degrees north.
ERROR_ LATITUDE _ELLIPSE	Latitudinal errors from the ellipse fitting.
DIAM_ELLIPSE_MAJOR	Major axis of a nonlinear least squares ellipse fit to the vertices in the DEM selected to identify the crater rim. Units: km.
ERROR_ELLIPSE_MAJOR	Errors of the major axis from the ellipse fitting.
DIAM_ELLIPSE_MINOR	Minor axis of a nonlinear least squares ellipse fit to the vertices in the DEM selected to identify the crater rim. Units: km.
ERROR_ELLIPSE_MINOR	Errors of the minor axis from the ellipse fitting.
ELLIPSE_ECCEN	Eccentricity of the nonlinear least squares ellipse fit, defined as $e = \sqrt{1 - b^2/a^2}$ (Robbins and Hynek, 2012b).
ELLIPSE_ ELLIP	Ellipticity of the nonlinear least squares ellipse fit, defined as $\varepsilon = a/b$ (Elbeshausen et al., 2013).
ELLIPSE_ANGLE	Tilt angle of the nonlinear least squares ellipse fit. The value is between − 90°and + 90°, 0° indicates to a major axis that is parallel to a line of latitude, and positive values are counter-clockwise. Units: degrees.
ERROR_ELLIPSE_ANGLE	Errors in deriving the azimuth of major axis in the ellipse fitting.
PTS_USED_ELLIPSE	Number of points selected around the crater rim to fit the crater with an ellipse.
RMS_ELLIPSE _FIT	RMS of fitting the crater with an ellipse. Units: m.
DEPTH_RIMFLOOR	The depth of the crater after topographic correction, see Section 3.2 for details.
DEPTH_DIAMETER_RATIO	The ratio of DEPTH_RIMFLOOR to DIAM_CIRCLE.

global mosaic of HAMO images, which was been imported into the ArcGIS software. In this process, we used a polar stereographic projection poleward 60° and a standard cylindrical projection for other latitudes. Subsequently, an ArcGIS extension, CraterTools (Kneissl et al., 2011), was used to determine the positions and measure the diameters of the impact craters. CraterTools works independently of the particular map projection of the image and it can fit a crater rim with a circle perfectly in many cases. The results were checked with the global mosaic of LAMO images where available to ensure the accurate positions of the manually identified points on the crater rims. Note that the craters were identified independently by each author and then cross-checked. In addition, previous results by Vincent et al. (2014), Marchi et al. (2012), and Kneissl et al. (2011) were also included after cross-checking, although the centers and diameters are not exactly the same. Therefore, the (4) Vesta crater database generated in this study is based on the aggregation of previous results.

More accurate crater rim traces were extracted based on the above initial fitted circle using the following automated algorithm, which was developed on the platform of ESRI's ArcGIS with the COM-based programming language of C#. Eight profiles crossing the circle center are created evenly with a 22.5° angular difference between neighboring profiles (Fig. 2). Then, a local maximum of the topographic curvature in each profile is found within 10% of the diameter on both sides of the initial circle. This method is similar to that by Vincent et al. (2014) except we use eight instead of four profiles; in addition, the method can remove this interference from other craters intersecting with the profiles (Fig. 2b; the black end points that intersect with other craters are considered invalid). To remove possible errors from the above automatic search (e.g., the crater rim may be modified by mass wasting, see Kneissl et al. (2011)), the end points are also manually checked to ensure that they are indeed along the crater rim. The result of this treatment is that there will be up to 16 points determined along the crater rim (i.e., rim points). Rim points are also manually added when necessary to ensure that each crater has at least six points. The resultant rim points are used to represent the crater rims in future for computing the reported crater parameters. Therefore, the crater database in this research essentially consists of manual results with automated refinements.

Most of the parameters in Table 1 are derived from the circle and ellipse fitting using the crater rim points defined using the techniques above. Circles were fit using a nonlinear least squares method, while ellipse fits were accomplished by a stable procedure prescribed by Fitzgibbon et al. (1999). To achieve reliable fits, the gross errors (larger than three times standard deviation in the initial circle and ellipse fitting) were removed.

We note that the above fittings are based on the local coordinate system, i.e., the rim points identified from images are first projected onto the ground plane (Fig. 3). This process is extremely important for measuring the depth of the craters considering that many craters on the surface of (4) Vesta are distributed over slopes (Kneissl et al. (2011); Vincent et al., 2014) and large topographic undulations commonly exist on the surface of (4) Vesta (Herrick et al., 2012). The process of this projection can be summarized as the following steps: (1) A ground surface is fitted with the rim points and the manually identified crater rim is projected in this plane; (2) The topographic information of the crater rim and the profiles are searched from the original DEM according this projection; (3) A local ground coordinate system, in which the origin is the crater center, x points local east, and y points local north, and z points up, is created and the topographic information is corrected to this coordinate system. The aim of this correction is to integrate the topographic data in the local ground coordinate system, which makes the measurements of depth and diameter exactly same with those measured in the fields. In the local corrected topographic data, the depth of each valid profile is measured as the elevation difference between the highest and lowest point. Finally, the crater depth is considered as the maximum depth among the depths of the valid profiles. Fig. 3 schematically displays three valid profiles (with valid rim points in two ends), and the maximum depth among them is the crater depth.

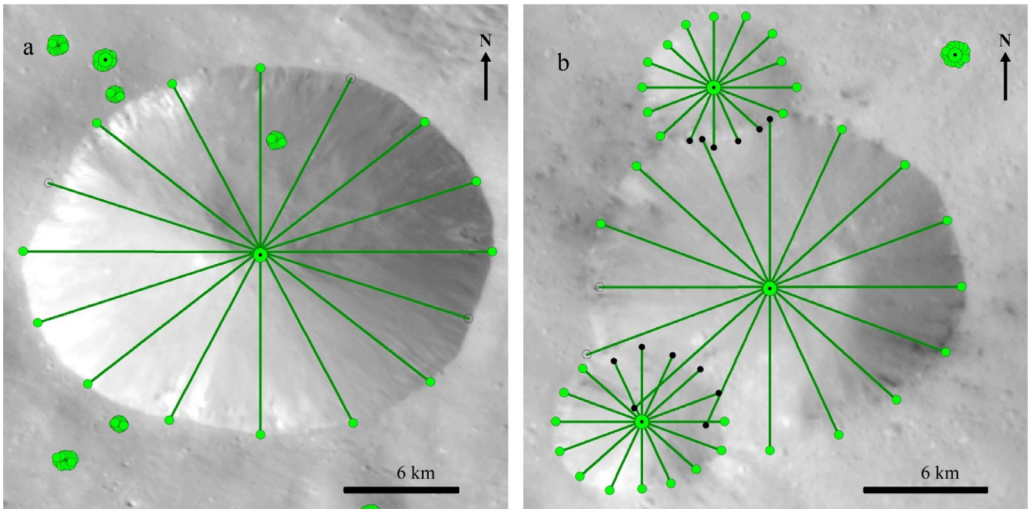

Fig. 2. Rim point identification in this research. (a) Rim points identified for the isolated Crater Sextilia (64.08°W, 39.00°S); the hollow circles are removed as gross errors before circle fitting; (b) Rim points identified for Crater Fulvia (67.49°W, 26.25°S) and two overlapping craters, in which the black points are considered invalid and the hollow circles are also removed as gross errors. The background is the HAMO mosaic.

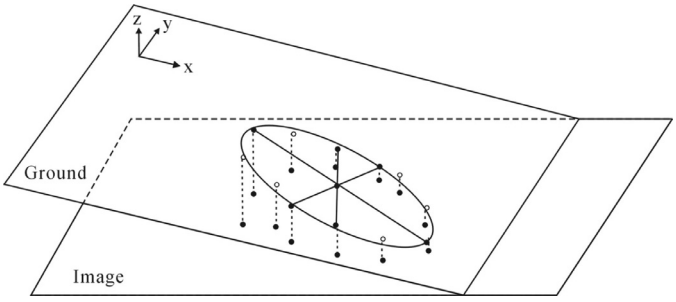

Fig. 3. Diagram for projecting rim points identified in the image onto the local ground plane. Rim points identified in the image are projected onto the ground surface within the local coordinate system and the profiles with valid rim points are used to derive the depth of the crater.

Fig. 4 shows the measurements to a crater located at 94.3°W, 32.8°N. To fit the crater with rim points, eight profiles (top) are used and the rim points are further modified as we described in the manuscript. To derive the depth of the crater, local ground plane is fitted with the DEM. All of the profiles (middle) will be then modified according to the local fitted ground plane. For example, profile 6 (solid line, bottom), the steepest profile, will be corrected to the dotted line. As a result, the depth measured from the corrected profile will be smaller than that from the original profile. The average depth of all these depths of the profiles is considered as the depth of the crater.

3.3. Uncertainties in measurements

The uncertainties come from both the measurements and the data source. As we stated above, the rim points were manually identified in the HAMO images and cross checked in the LAMO images where available. Therefore, the error in identifying the rim points can be considered as one pixel, which is equivalent to 60 m for HAMO, or $\sigma = \pm 30$ m. The depth of the crater is measured as the elevation difference between the two points in DEM, and its measurement error can be calculated from the error propagation law as

$$\sigma_h = \sqrt{\sigma_1^2 + \sigma_2^2} = \sqrt{6^2 + 6^2} = 8.48\,\text{m}$$

where σ_1 and σ_2 represent the elevation errors of the two points in DEM, respectively. However, it is necessary to note that the above ideal derived measurement error is only appropriate providing the terrain is very smooth, and it will be much larger in rugged regions, especially considering that the spatial resolution of DEM is ~70 m/pixel.

4. Results and analyses

4.1. Database completeness analyses

The mosaics used in this research almost globally cover the surface of (4) Vesta, providing a reliable basis for the creation of the crater database. The completeness diameter of the database, i.e., the smallest diameter for which all craters were identified, can be determined from the crater size-frequency distribution (e.g., Robbins and Hynek, 2012b; Salamunićcar et al., 2011). The philosophy behind the strategy is that the crater population will continue to increase in number as size decreases, and any observed dramatic and sudden decrease is most likely due to the inability to identify craters near the resolution limit of the imaging rather than a property of the surface (Robbins and Hynek, 2012b). Therefore, we first performed a global analysis of the crater database using an incremental size-frequency distribution plot binned in $2^{1/2}D$ intervals (Fig. 5) based on a method recommended by the Crater Analysis Techniques Working Group (1979).

Currently, only Marchi et al. (2012) have globally mapped craters on the surface of (4) Vesta, to the best of our knowledge. Marchi et al. (2012) published 1872 craters with diameters ≥ 4 km based on a mosaic with a resolution of 260 m covering ~80% of Vesta's surface. They also mapped 3809 additional craters larger than 1.0 km in diameter distributed over the entire surface of (4) Vesta (personal communication). Fig. 5 also includes their results, which indicate that the peak diameter of the crater population is about 4.0 km. In general, our mapped database is very consistent with that of Marchi et al. (2012) for craters larger than 4.0 km in diameter, and the inconsistency for craters between 10 and 14 km is mostly caused by the differences of the measured diameters instead of a deficiency in crater numbers.

According to the above philosophy, the completeness diameter of our crater database can be considered to be 0.7 km. However, Robbins et al. (2014) indicated that the level of agreement among experts in identifying craters and the completeness diameter also depends on many other factors including terrain type, number of craters per diameter bin, and crater diameter. As a

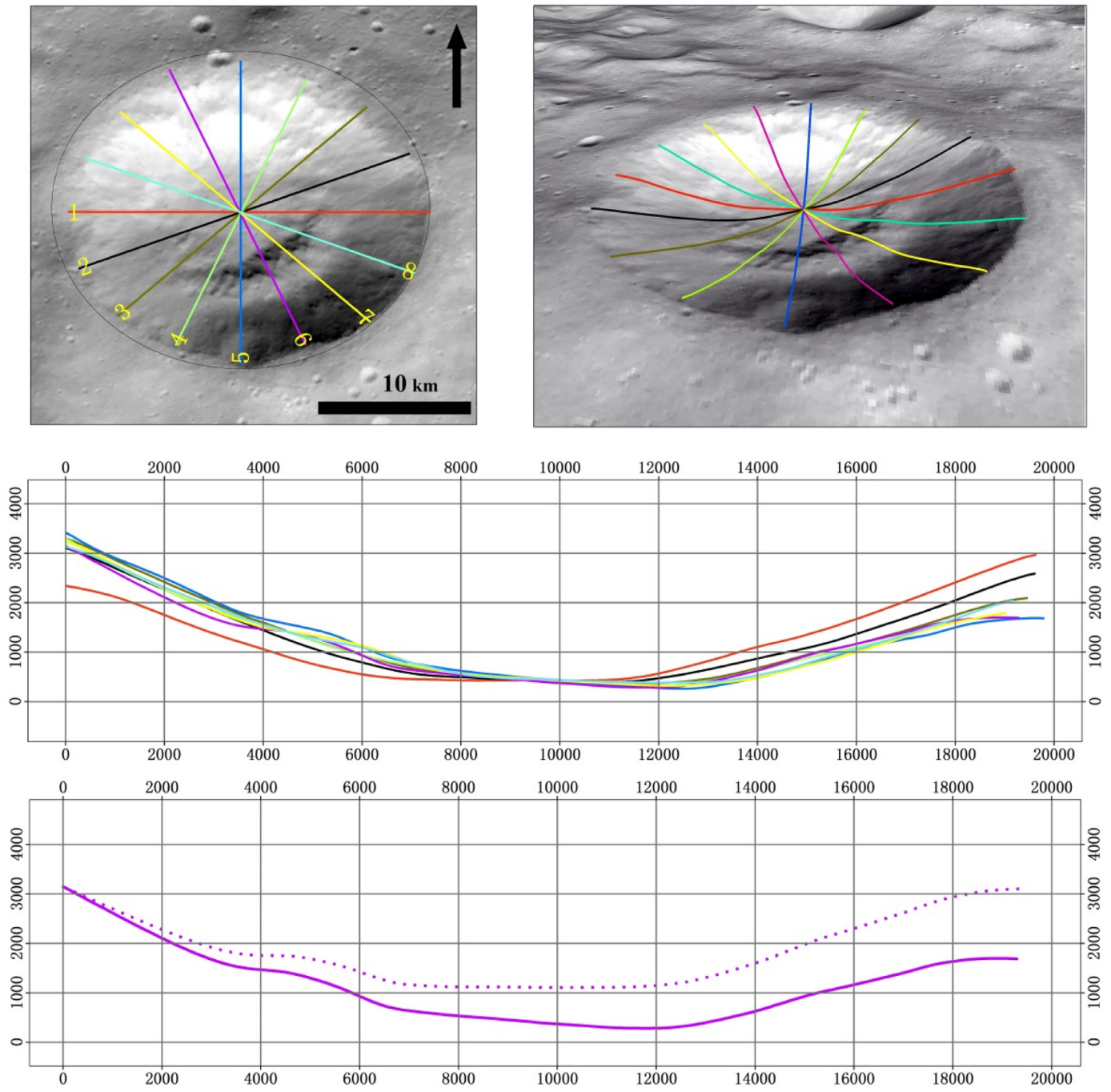

Fig. 4. The depth and dismeter measurements to a crater located at 94.3° W, 32.8° N.

result, there could be a few other craters larger than 0.7 km in diameter left in our crater database. However, this analysis is also significant in related analyses, or at least it can provide a basis for small craters mapping and analyses in future. Our database contains 11,605 craters ($D \geq 0.7$ km), which also form the base for the subsequent analyses in this research. The entire database has an additional 9293 craters ($D < 0.7$ km) that may be obtained by contacting the corresponding author.

4.2. Global distributions of craters

Fig. 6 shows the global distribution of the 11,605 mapped craters with $D \geq 0.7$ km in this research. Fig. 6a shows fitted circles overlaid on the HAMO global mosaic, and Fig. 6b shows their spatial density, i.e., the number of craters per 10^4 km^2, by averaging over the 100×100 km rectangle centered at the current pixel. It is obvious that the area around Crater Marcia (20.24 °W, 9.72 °N, $D = 56.70$ km) is less populated (Fig. 6b), which we interpret to be because the crater and its ejecta destroyed or covered over previously existing craters. The crater densities in the two polar regions are also lower than in other regions, which is presumably mostly caused by erosion from large young craters (e.g., Rheasilvia Basin in the south, and Crater Albana in the north), although omissions due to the poor illumination of the images is also possible. There are several regions, as indicated in Fig. 6b, which are particularly densely populated by craters.

Fig. 7 shows the crater center distribution with respect to elevation. Craters on the surface of (4) Vesta are distributed from

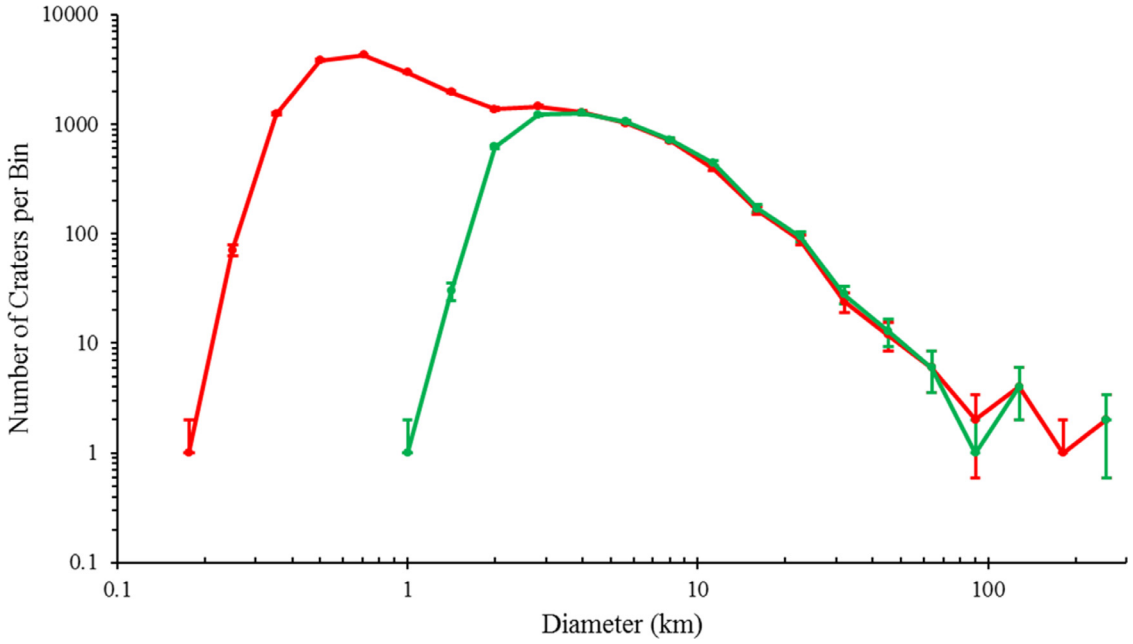

Fig. 5. Incremental size-frequency distribution plot of the global craters (in red) compared with that obtained by Marchi et al. (the complete database, personal communication; in green), binned in $2^{1/2}$ D intervals. The crater diameter is derived by circle fitting using rim points. The result indicates that the peak number for our crater database is about 0.7 km in diameter.

−22.0 km to 19.0 km, and we binned the craters every 1 km in the topographic range. Generally, similar to the distribution pattern found by Marchi (2002) for the density of craters $D \geq 4.0$ km, highland areas usually have a higher crater density. Our histogram further reveals that there are 7561 (~65.15%) craters distributed in areas higher than 0 m (see Preusker et al. (2014) for the reference plane).

4.3. Morphometric parameters of the craters

A by-product of the completeness analyses is the diameter distribution pattern for the crater database in this research. Fig. 5 clearly shows that the number of craters increases as their diameter decreases from 64 km to 4 km as a power-law relationship. For craters with diameter from ~2.8 km to 1.4 km, their numbers do not increase as rapidly as for larger craters. When the diameter is smaller than 1.4 km, the crater population again steeply increases. These trends are similar to those in the regional crater distribution model (Marchi et al., 2014), although there is no interpretation currently.

Fig. 8 shows a plot of the number of craters with depths > 0.1 km in which the crater depths are binned every 0.1 km. There are 4637 craters included in the analyses. Among these craters, 4406 craters (~95.0%) are less than 1.0 km in depth. Crater Tarpeia is the deepest with a depth of ~5.0 km. Fig. 8 also indicates that the trend in the number of craters deeper than 1.0 km fluctuates, and this is more evident for the deeper craters. However, for those craters less than 1.0 km in depth, the number of craters increases steadily when the depth decreases. The fitted power function is as follows:

$$N = 419.9 \times d^{-0.73} - 421.9\left(R^2 = 0.9952\right), \quad (17)$$

where N is the number of craters for each bin, and d is the depth of the left border (the smaller value) of the corresponding bin.

For the 4637 craters for which $d \geq 0.1$ km, the mean value of d/D, i.e., the ratio of the depth to diameter of crater, is 0.065 ± 0.023. Fig. 9 shows a histogram of the ratio d/D of the 4637 craters binned in 0.01 increments of d/D. The peak of the distribution is between 0.05 and 0.06, and there are 4225 craters (91.1%) with a d/D of less than 0.10. Fig. 10 shows the variation in d/D of craters with a particular diameter. The d/D of craters less than 40 km in diameter varies from 0.02 to 0.16 with a mean value of 0.065 ± 0.02; however, for the larger craters, this value clearly decreases.

To obtain a reliable statistic for the ellipticity of the craters, we first removed the results with large relative errors in the ellipse fitting (i.e., σ_0 divided by the length of the major axis of the fitted ellipse must be less than 0.20), and we further removed craters for which fewer than 10 points were used to fit the ellipse. Finally, we only selected craters larger than 2.0 km and $\varepsilon > 1.12$ (see Fig. 3 in Robbins and Hynek, 2012a). As a result, 742 craters are included in the calculation. Fig. 11a shows the histogram and Fig. 11b shows the distribution with respect to crater diameter. It can be seen that craters with an ellipticity larger than 1.2 are those craters less than 50 km in diameter, indicating that the ellipticity is less affected by the slope and impact angle in the formation of large craters. For craters less than 20 km in diameter the ellipticity varies greatly, which is probably because the factors contributing to the ellipse craters' formation play much more important role in the formation of small craters than large craters.

Fig. 12 presents a histogram of the azimuths of the major axis of the craters shown in Fig. 11. The mode of their distribution is generally uniformly distributed in different directions, except for craters with azimuths of −90° to −80°, −40° to −30°, 30°–40°, and 50°–70°, which are relatively lower to the mean in number. In addition, craters with azimuths of −20° to −10° are most densely distributed. If the azimuths of major axis were consistent with the impact direction, the results implicate that (4) is almost randomly bombarded by projectiles.

5. Comparison with previous studies

5.1. Comparison with previous results

Focusing on the study of the d/D of craters across the surface of (4) Vesta, Vincent et al. (2014) selectively mapped 1025 craters

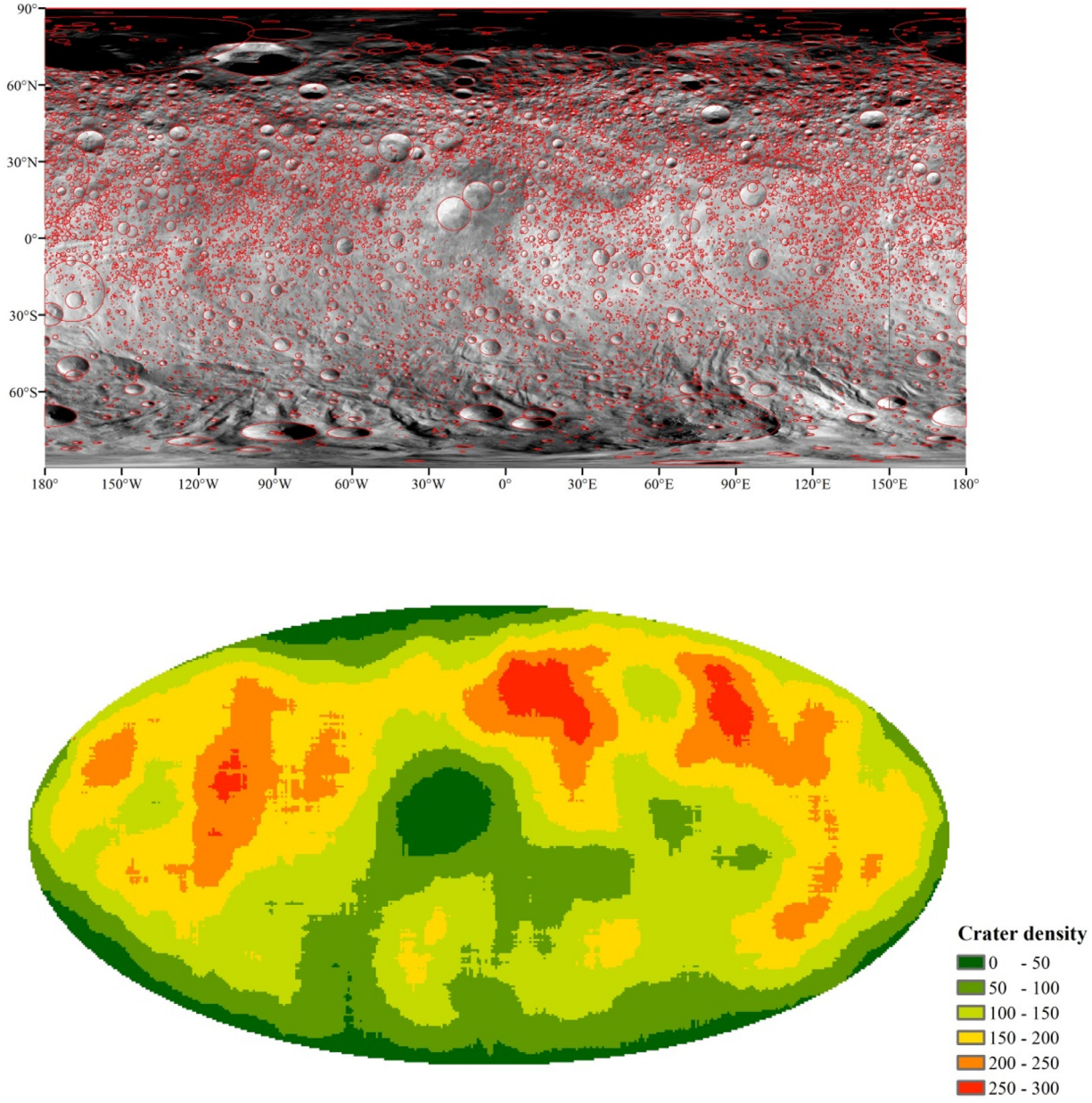

Fig. 6. Global distribution of craters on the (4) Vesta surface. (a) Top panel: global crater distribution as a simple cylindrical projection; (b) bottom panel: the density map of all craters with a $D \geq 0.7$ km as a Mollweide projection (in number of craters per 10^4 km^2), which ensures that the crater density was calculated over the same area at different latitudes.

ranging from 1.5 to 64 km in diameter. Their results show that d/D has the range 0.05–0.35 and a mean value of 0.17 ± 0.01. Moreover, there are two peaks at 0.15 and 0.19 in the histogram presented by Vincent et al. (2014). In our crater database, there are 6297 craters larger than 1.5 km in diameter, among which there are 4635 craters deeper than 0.1 km, almost the same as the selected craters shown in Fig. 10. The maximum d/D of those craters is 0.16 with a mean value of 0.065 ± 0.023, and there is only one peak at 0.04–0.05, instead of two peaks in the results by Vincent et al. (2014). In addition, there are 22 craters with obvious ejecta among these craters in this study. Moreover, the mean value of the d/D of these 22 craters is 0.100 ± 0.021, which is also less than the value obtained by Vincent et al. (2014). The difference between our results and those of Vincent et al. (2014) arises mainly from the DEM used in deriving depth. Moreover, a product obtained using stereo-photoclinometry is used in their research, which is usually with great uncertainties (Bourke et al., 2006), while a product obtained using stereo-photogrammetry is used in our research. Another reason for the difference is that many degraded craters are included in our crater database, which will have a smaller d/D relative to other craters.

To verify our results, a method of shadow measurements, which was used in earlier studies and can give a rough information of the crater depth (see Melosh, 1989), was applied to four craters with the calibrated DAWN data (https://sbn.psi.edu/pds/resource/dawn/dwnvfcL1.html). Fig. 13 shows two images in which four craters were selected to measure the depth with the method of shadow measurements. The measurements are based on local coordinate system. Table 2 lists the related information to the images and selected craters. It is clear that our results are much closer to the shadow measurements than that of Vincent et al. (2014). The difference between our results and the shadow measurements are mainly due to the fact that the rim shadow doesn't exactly pass through the crater center. Therefore, our stereo-photogrammetry

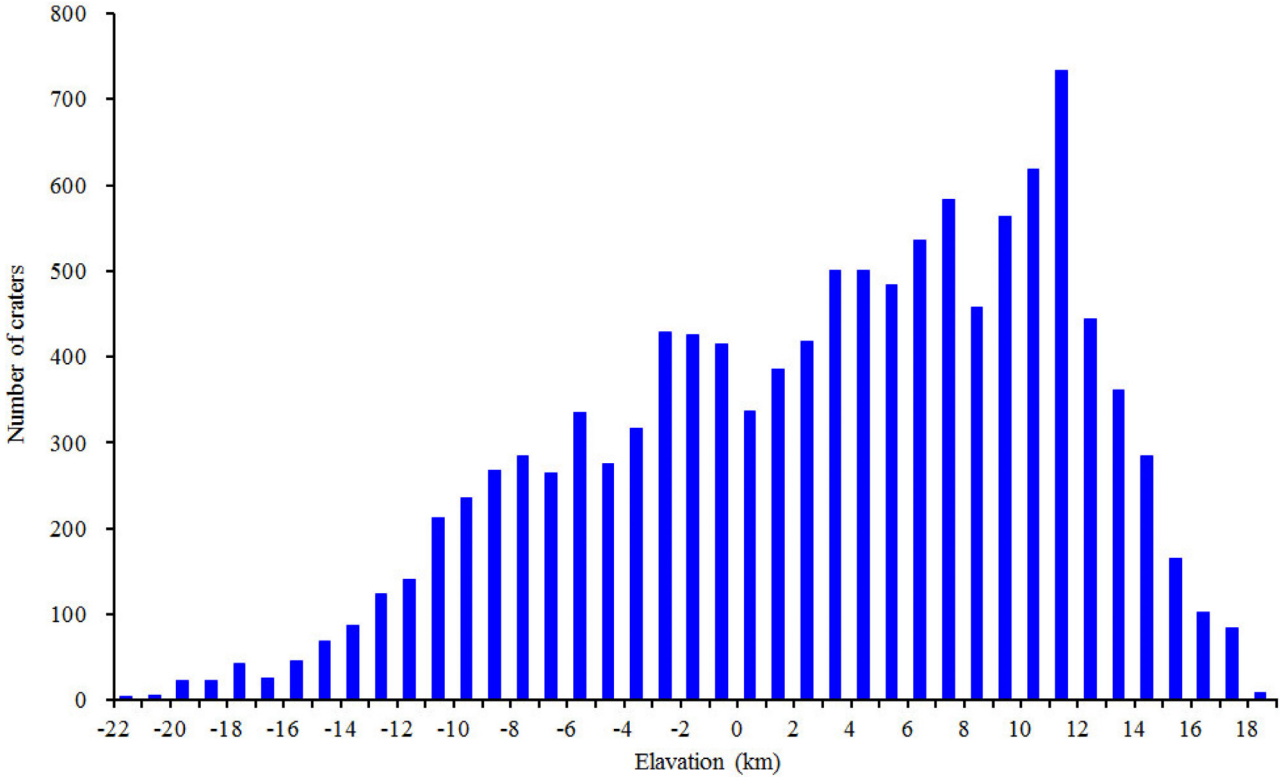

Fig. 7. Global distribution of crater centers with respect to the topography on the (4) Vesta surface. The crater center refers to the fitted circle center with rim points. In this histogram, the craters are binned from −22.0 km to 19.0 km every 1.0 km, and the elevation refers to the left border (the smaller value) of each bin.

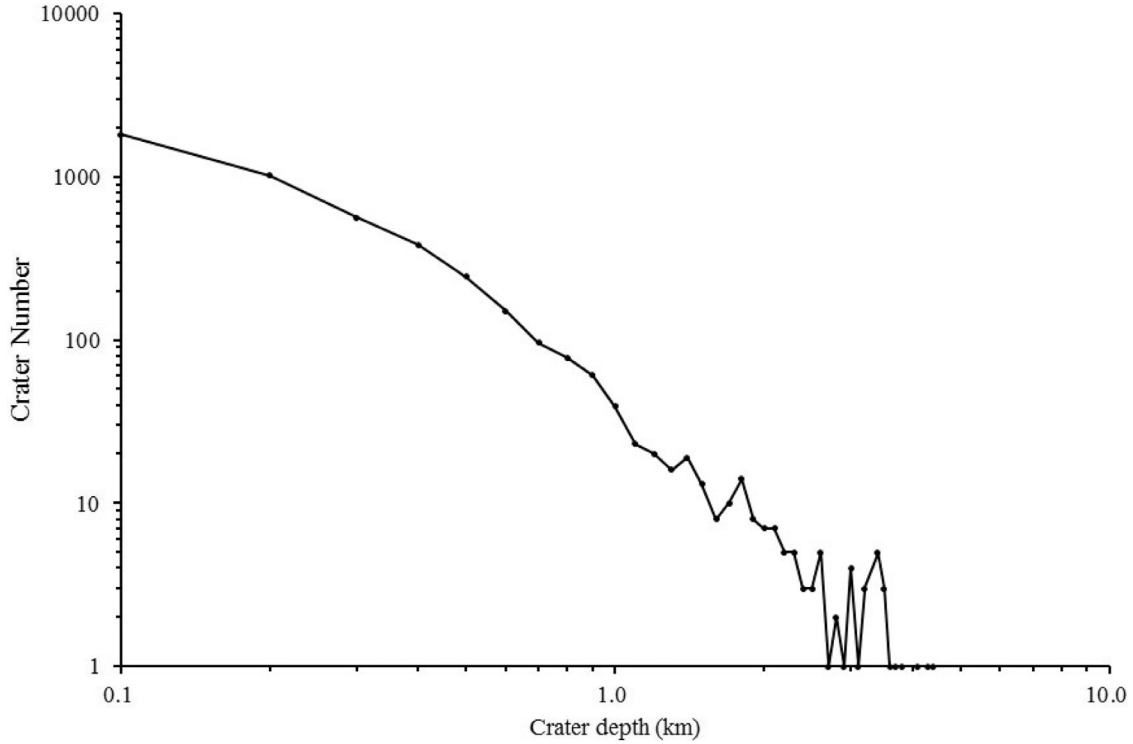

Fig. 8. Global distribution of crater depth for $d \geq 0.1$ km on the (4) Vesta surface. There are 4637 craters included in the analyses, and most of them (~95.0%) are less than 1.0 km in depth. Craters are binned from 4.5 km to 0.1 km every 0.1 km, and the crater depth refers to the left border (the smaller value) of the bin.

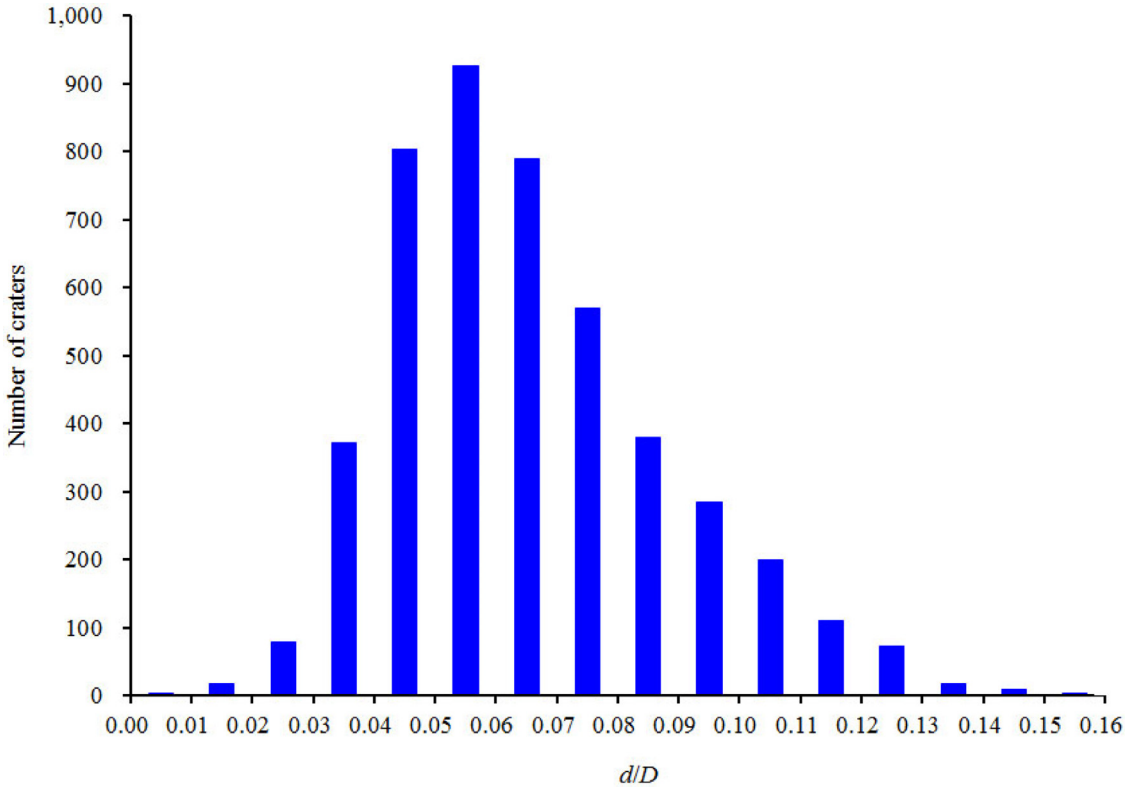

Fig. 9. Histogram of the d/D ratio of the 4637 craters for which $d \geq 0.1$ km. The peak of the distribution is between 0.05 and 0.06, and there are 4225 craters (91.1%) with a d/D of less than 0.10.

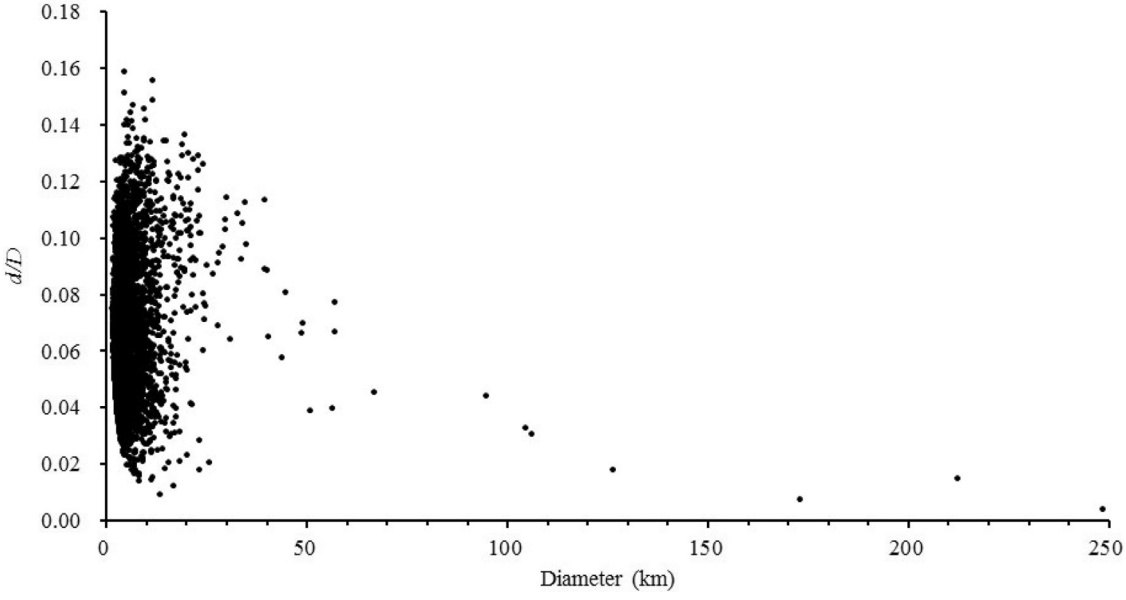

Fig. 10. Relationship between the ratio of d/D and diameter of the 4637 craters ($d > 0.1$ km) on the (4) Vesta surface.

Table 2
Information for the shadow measurements to the craters in Fig. 13.

Image No.	tm-FC21B0007808_11274122624F6F1		tm-FC21B0011757_11300022743F2C1	
Incidence angle (°)	80.10		79.61	
Crater ID	A	B	C	D
Rim shadow length (m)	13,134.36	10,435.17	12,557.61	11,548.85
Crater depth from shadow measurements (m)	2293.13	1821.88	2302.29	2117.34
Crater depth in our results (m)	2311.69	1913.24	2170.60	2258.66
Absolute relative error to our results (%)	0.80	4.78	6.07	6.26
Crater depth by Vincent et al. (2014) (m)	4471.55	4113.84	4249.34	4023.91
Absolute relative error to Vincent et al. (2014) (%)	95.00	125.80	84.57	90.05

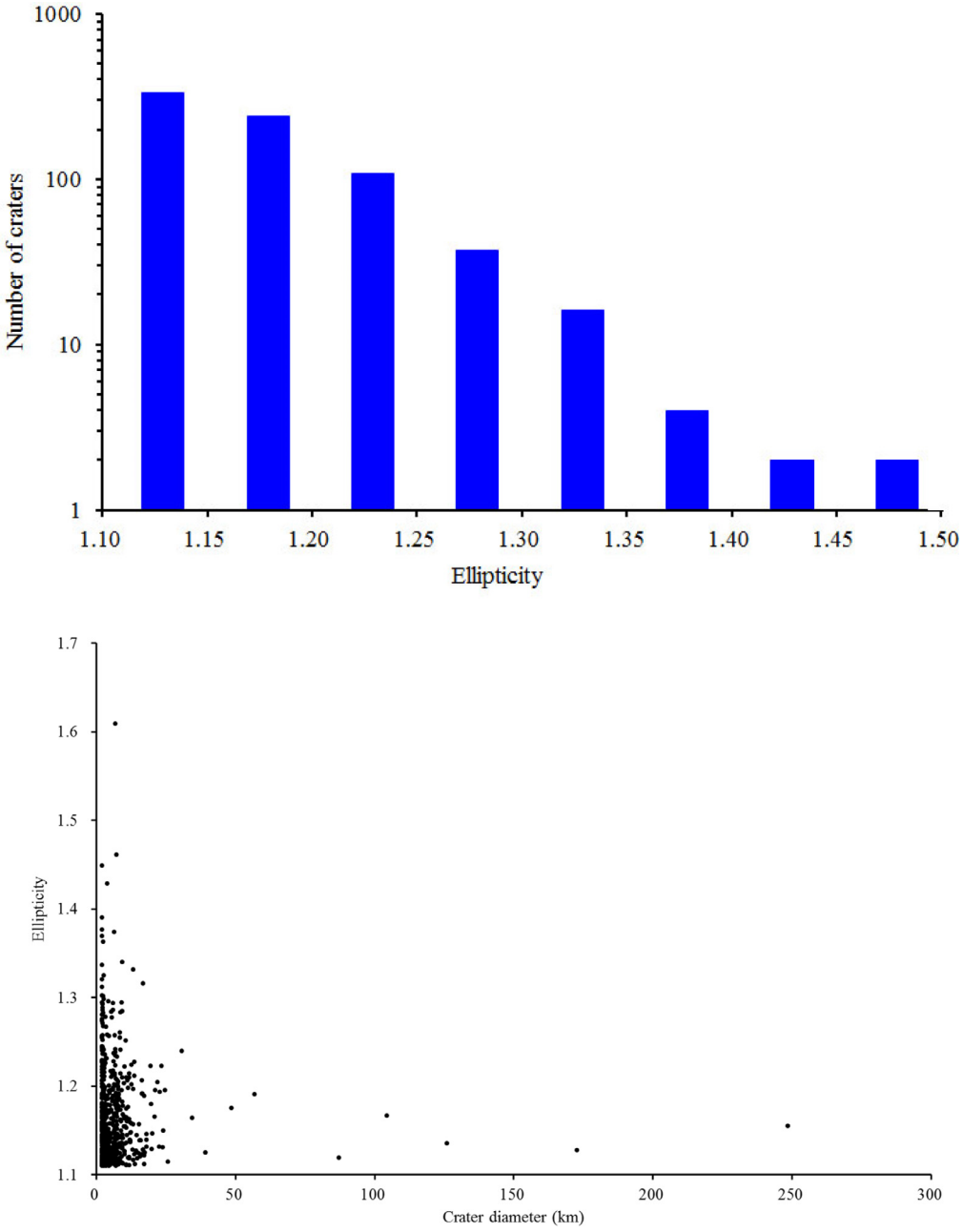

Fig. 11. Histogram of the ellipticity > 1.12 of the selected 742 craters, generated from ellipse fittings for craters with diameters larger than 2.0 km that used no fewer than 10 rim points and had small relative residual errors. (a) Top figure: Ellipticity versus crater number; (b) bottom figure: ellipticity versus crater diameter (obtained from fitted circles).

based statistic can lead to a reliable and comprehensive analysis of the crater morphology.

5.2. Comparison with craters on other bodies

The relationship of crater depth d and diameter D has been widely used to describe the shape of craters. It is often simply combined into the ratio d/D, and a power law with the form of $d = c_1 D^{c_2}$ has also been used. However, for simple craters on terrestrial planets, c_2 usually approaches 1.0 (e.g., Pike, 1974, 1980; Cintala and Mouginis-Mark, 1980), and then c_1 is equivalent to d/D. In earlier studies, Pike (1974) measured 204 fresh lunar craters smaller than about 15 km in diameter and derived that the parameter of d/D is about 0.2, which was accepted in many studies (e.g., Wood and Anderson, 1978; Melosh, 1989). This parameter is similar for simple craters on other terrestrial planets such as Mars (e.g., Pike, 1980; Cintala and Mouginis-Mark, 1980) and Mercury (Barnouin et al., 2012). However, d/D is ~0.11 for the fresh secondary craters on the Moon (Pike and Wilhelms, 1978) and is ~0.08 for such craters on Mars (McCord et al., 2012). Therefore, the d/D of the fresh craters on the surface of (4) Vesta is similar to those of the secondaries on the Moon and Mars, assuming our stereo-photogrammetry measurements are correct. In addition, we speculate that the seismic shaking of the asteroid from later impacts results in a difference in the mean values of d/D for craters on the surface of (4) Vesta compared with those on the Moon and Mars, as studied before (e.g., Asphaug and Melosh, 1993; Greenberg et al., 1996; Richardson et al., 2005). As a result, the crater diameter increases while the depth decreases, and these two effects jointly lower the value of d/D.

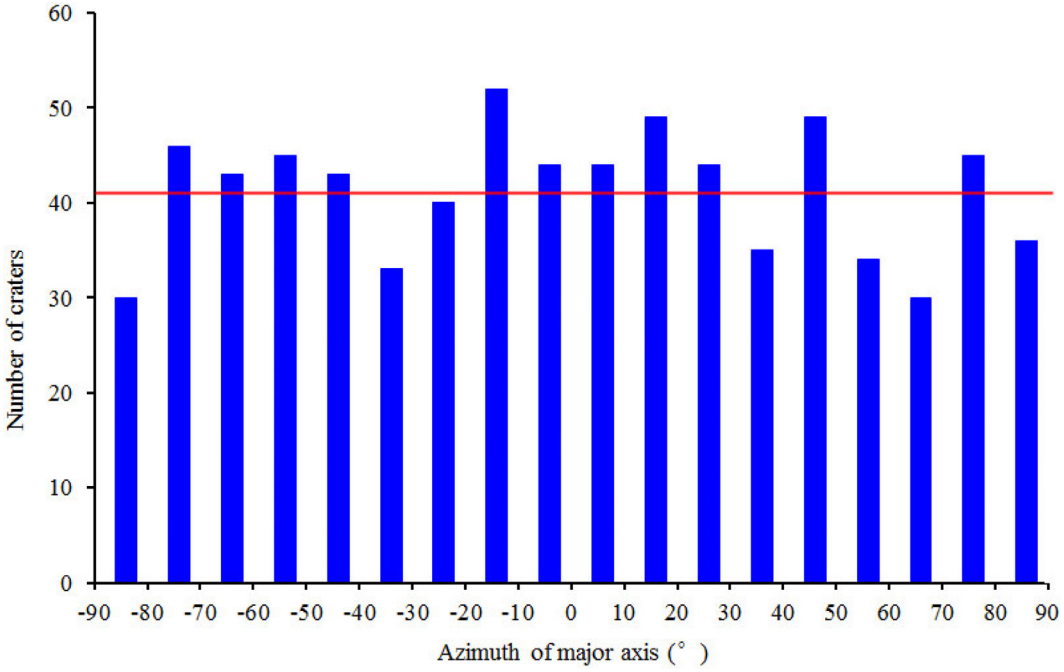

Fig. 12. Histogram of the azimuths of the major axis of the 742 craters shown in Fig. 11. The azimuths of the craters are binned every 10° from −90° to 90° The horizontal line indicates the mean value of the number of craters.

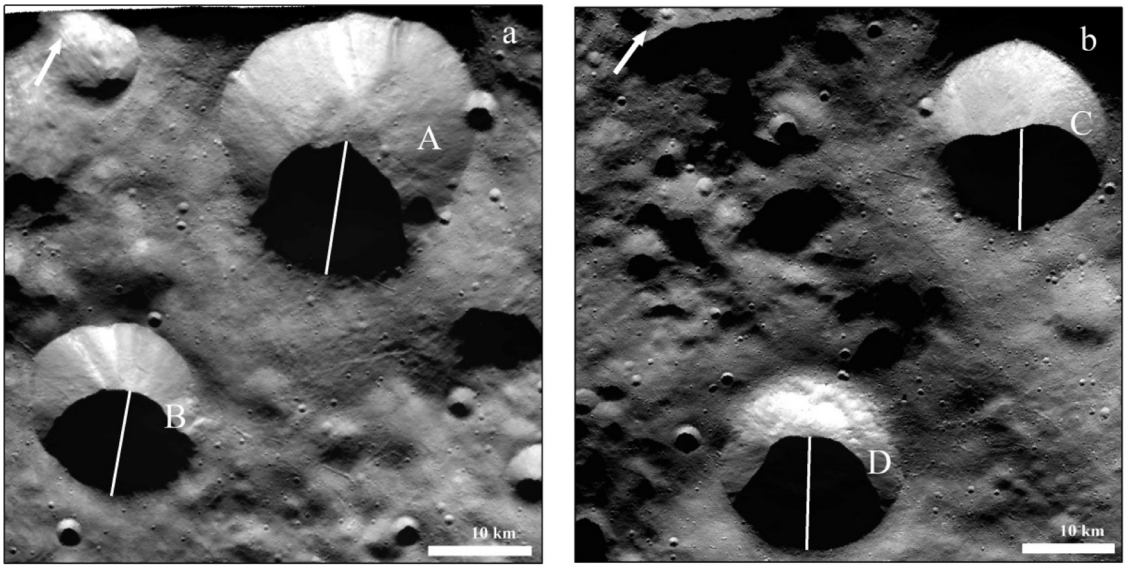

Fig. 13. Shadow measurements to the depth of four craters in calibrated DAWN images, and the measurements are based on local coordinate system. Craters A, B, C, and D are selected for shadow measurement, in which the white lines represent the shadow of the rim. The information of the images and crater measurements are listed in Table 2.

As to the small bodies (Table 3), Carr et al. (1994) measured the depth and diameter of craters on (951) Gaspra and found that parameter d/D varies from ~0.03 to ~0.125. Sullivan et al. (1996) analyzed the morphologies of craters on (243) Ida, and derived a d/D of ~0.025 to ~0.15 with the highest values corresponding to the fresh craters. However, the above two measurements were carried out using photoclinometry with considerable uncertainties (e.g., the error bars might be 20% for crater depths and 10% for crater diameters, Sullivan et al., 1996). Thomas et al. (1999) found the d/D of a few available craters on (253) Mathilde varying from ~0.12 to ~ 0.25, however, the uncertainties were at least 25%. Robinson et al. (2002) mapped the craters on the surface of (433) Eros and obtained their depths mostly by shadow measurements; they estimated the d/D of these craters to be 0.13 ± 0.03, although the freshest craters approach ~0.2. Shingareva et al. (2008) measured six craters from 1.8 to 8.6 km in diameter on the surface of Phobos using five stereo pairs of images from the High Resolution Stereo Camera of the Mars Express and concluded that their d/D varies from 0.15 to 0.24. Hirata et al. (2009) identified 38 craters on the surface of (25143) Itokawa and measured the depth as the distance from the center of the crater to the extrapolated surface according to the surrounding curvature. They then derived a d/D of 0.08 ± 0.03 with uncertainties of ~25% for large craters or 0.1–0.3 m for smaller craters using the estimated depth. Vincent et al. (2012b) measured the depths of 125 craters on the surface of (21) Lutetia according to the shadows, and found that their d/D of these craters varies from 0.05 to 0.3 with a peak at ~0.12. Besse et al. (2012) mapped 46 craters on the surface of (2867) Steins

Table 3
Statistics of d/D of simple craters for different bodies.

Object		d/D	Reference
Rocky bodies	Moon, Mars, Mercury	0.2	(Barnouin et al., 2012; Pike, 1974; Pike, 1980)
	Gaspra	0.125[a]	(Carr et al., 1994)
	Ida	0.154[a]	(Sullivan et al., 1996)
	Mathilde	0.12–0.25	(Thomas et al., 1999)
	Eros	0.13 ± 0.03	(Robinson et al., 2002)
	Phobos	0.15–0.24	(Shingareva et al., 2008)
	Itokawa	0.08 ± 0.03	(Hirata et al., 2009)
	Lutetia	0.12[b]	(Vincent et al., 2012b)
	Steins	0.055–0.2	(Besse et al., 2012)
	Ceres	0.06 ± 0.04	(Gou et al., 2017)
	Vesta	0.168 ± 0.01	(Vincent et al., 2014)
	Vesta	0.065 ± 0.023	This study

[a] Fresh craters.
[b] Peaks of statistic.

ranging from 150 to 2100 m in diameter and derived that the d/D of these craters varies from 0.04 to 0.25 with a center of 0.10. Recently, Gou et al. (2018) made a global catalogue of Ceres impact craters and derived the d/D of fresh craters, which are 0.11 ± 0.04 and 0.06 ± 0.04, respectively. They also used DEMs produced using stereo-photogrammetry and the same techniques presented here. Therefore, the results of the Vestan craters derived in this research is generally consistent with those craters on the surface of Ceres and (25143) Itokawa, although smaller than most of the craters on other small bodies.

We speculate the following reasons for this difference: (1) The depths of the craters on other small bodies are mostly based on results using the photoclinometry method, which usually leads to large uncertainties. Some uncertainties cannot even be estimated, as pointed out by the above studies. In contrast, our results are based on the photogrammetry method using stereo images, which is more reliable in measuring depth. (2) There are usually a few simple craters that can be distinguished from the available images in the above studies, and some more degraded craters may be discovered if high resolution images are provided. These degraded craters will decrease the mean value of d/D of the craters. (3) In most of the above studies, topographic correction is not considered when measuring crater depth, which would greatly lower the ratio of d/D, especially for craters on small bodies.

Bottke et al. (2000) investigated nine lunar maria regions and found that ~5.4% of the surveyed craters had an $\varepsilon \geq 1.2$, and this fraction does not change significantly with size. For craters larger than 1.7 km on Venus, Bottke et al. (2000) found the fraction was up to 22% for $\varepsilon \geq 1.2$, while it drops to 14% for craters with diameters $D \geq 20$ km and then remains unchanged for larger values of D. According to the Mars crater database by Robbins and Hynek (2012a), there are 205,249 (53.40%) with $\varepsilon \geq 1.1$, 66,441 (17.29%) craters with $\varepsilon \geq 1.2$, and 24,644 (6.41%) craters with $\varepsilon \geq 1.3$ out of a total of 384,343 craters. Generally, the fraction of craters with $\varepsilon \geq 1.2$ is similar for the lunar maria and surface of (4) Vesta, while it is more for Venus and Mars. However, when surveying craters on lunar maria, Bottke et al. (2000) excluded those craters within obvious rays, which are probably secondaries and usually have higher ε (one salient difference between primary and secondary craters is circularity; Pike and Wilhelms, 1978), which would artificially bring the value lower than that for Venus and Mars, which do not exclude any measured craters. Thus, the reason for the difference between Vesta and other worlds is probably because few secondaries exist on the surface of (4) Vesta due to the relative low escape velocity.

6. Conclusions

The aim of this work was to create a global database of the craters on (4) Vesta and perform some initial statistical and morphometric analyses. Based on the results of a completeness analysis, 11,605 craters larger than 0.7 km (10 pixels in the HAMO mosaic) in diameter were included in this database. Initial analyses of the global distribution, diameter, ellipticity, azimuth of the major axis of the fitted ellipse, depth, and d/D were performed. There are several areas with high concentrations in the distribution of these craters, while the polar regions and the area near Crater Marcia are less populated. We developed a method to precisely measure the diameter and depth by considering local topographic correction, and other parameters were derived by fitting the identified rim points with a circle and ellipse. Our measurements show that the d/D on the surface of (4) Vesta is similar to that found on (25143) Itokawa and is smaller than that of craters on other solid bodies. The fraction of craters with an ellipticity larger than 1.1 or 1.2 is less than it is for craters on the Martian surface, which is attributed to the fact that few secondary craters exist on the surface of (4) Vesta. In addition, the azimuth of the fitted ellipses for the craters is approximately uniformly distributed, indicating that the impact angles are consistent with being random.

The database of the global craters of (4) Vesta has a variety of potential applications, such as geologic mapping and as tracers for surface processes. Moreover, it can play an especially important role in age dating, which is a task we plan to do in the near future.

Acknowledgments

The authors gratefully acknowledge the NASA Dawn Science and Flight teams and the instrument teams for providing HAMO, LAMO, and DTM data products, which were downloaded from the website https://sbn.psi.edu/pds/resource/dwnvfc2.html. The authors thank Ottaviano Ruesch and another anonymous reviewer for their comments and suggestions for the improvement of the manuscript. The authors also thank Thomas Kneissl for the CraterTools software. In addition, the authors want to give special thanks to Jean-Baptiste Vincent, Simone Marchi, and Katrin Krohn for sharing their Vestan crater databases, and to Stuart Robbins for sharing his Martian crater database and his advice for displaying the ellipticity and azimuths of craters. This work was supported by the National Natural Science Foundation of China (Grant Nos. 41490635 and 41472303), the Strategic Priority Research Program of the Chinese Academy of Sciences with the project "Digital Moon and Earth- Moon System Evolution", and by the opening fund of the Lunar and Planetary Science Laboratory, MUST—A Partner Laboratory of the Key Laboratory of Lunar and Deep Space Exploration, CAS(Macau FDCT Grant No. 039/2013/A2).

Appendix A. Uncertainties in the circle- and ellipse-fit parameters

Many parameters in this crater database are from circle- and ellipse-fittings, and the uncertainties of these parameters are derived below.

Denoting the central location and radius of the fit circle by $(\hat{\alpha}, \hat{\beta})$ and $\hat{R}$, the perpendicular distances from the identified rim points to the circle are:

$$v_i = \sqrt{\left(x_i - \hat{\alpha}\right)^2 + \left(y_i - \hat{\beta}\right)^2} - \hat{R}. \tag{A.1}$$

This equation can be linearized as follows:

$$v_i = \sqrt{x_i^2 + y_i^2} + \frac{\partial v}{\partial \hat{a}}\hat{a} + \frac{\partial v}{\partial \hat{b}}\hat{b} + \frac{\partial v}{\partial \hat{R}}\hat{R}. \tag{A.2}$$

The above equation is rewritten in matrix form as:

$$V = B\hat{x} - L, \tag{A.3}$$

where $V = \begin{bmatrix} v_1 \\ \vdots \\ v_n \end{bmatrix}$,

$$B = \begin{bmatrix} \left(\frac{\partial v}{\partial \hat{\alpha}}\right)_1 & \left(\frac{\partial v}{\partial \hat{\beta}}\right)_1 & \left(\frac{\partial v}{\partial \hat{R}}\right)_1 \\ \cdots & \cdots & \cdots \\ \left(\frac{\partial v}{\partial \hat{\alpha}}\right)_n & \left(\frac{\partial v}{\partial \hat{\beta}}\right)_n & \left(\frac{\partial v}{\partial \hat{R}}\right)_n \end{bmatrix},$$

$$\hat{x} = \begin{bmatrix} \hat{\alpha} \\ \hat{\beta} \\ \hat{R} \end{bmatrix},$$

and $L = -\begin{bmatrix} \sqrt{x_1^2 + y_1^2} \\ \cdots \\ \sqrt{x_n^2 + y_n^2} \end{bmatrix}$.

When fitting the circles, the principle is to minimize the sum of squares of v_i, i.e.,

$$V^T V = \sum_{i=1}^{n} v_i^2 = \min. \tag{A.4}$$

The errors of the resultant $(\hat{\alpha}, \hat{\beta})$ and $\hat{R}$ can be calculated according to the error propagation law:

$$\hat{\sigma}_{\hat{X}} = \hat{\sigma}_0 \sqrt{Q_{\hat{X}\hat{X}}}, \tag{A.5}$$

where $\hat{\sigma}_{\hat{X}}$ has three elements denoting the error of $\hat{\alpha}$, $\hat{\beta}$, and $\hat{R}$. Moreover, $\hat{\sigma}_0$ is the standard error of a unit weight, $Q_{\hat{X}\hat{X}}$ is the cofactor matrix, and they are respectively calculated as follows:

$$\hat{\sigma}_0 = \sqrt{\frac{V^T V}{n-3}}, \tag{A.6}$$

$$Q_{\hat{X}\hat{X}} = \left(B^T B\right)^{-1}. \tag{A.7}$$

The errors from ellipse fitting can be derived using a similar method. In ellipse fitting, the residual from each rim point to the resultant quadratic polynomial is:

$$v_i = \hat{a}x_i^2 + \hat{b}x_i y_i + \hat{c}y_i^2 + \hat{d}x_i + \hat{e}y_i + \hat{f}. \tag{A.8}$$

This equation can be linearized as follows:

$$v_i = \frac{\partial v}{\partial \hat{a}}\hat{a} + \frac{\partial v}{\partial \hat{b}}\hat{b} + \frac{\partial v}{\partial \hat{c}}\hat{c} + \frac{\partial v}{\partial \hat{d}}\hat{d} + \frac{\partial v}{\partial \hat{e}}\hat{e} + \frac{\partial v}{\partial \hat{f}}\hat{f}. \tag{A.9}$$

We rewrite it in the form of Equation (A.3) again, and the corresponding matrices are:

$$V = \begin{bmatrix} v_1 \\ \vdots \\ v_n \end{bmatrix},$$

$$B = \begin{bmatrix} \left(\frac{\partial v}{\partial \hat{a}}\right)_1 & \left(\frac{\partial v}{\partial \hat{b}}\right)_1 & \left(\frac{\partial v}{\partial \hat{c}}\right)_1 & \left(\frac{\partial v}{\partial \hat{d}}\right)_1 & \left(\frac{\partial v}{\partial \hat{e}}\right)_1 & \left(\frac{\partial v}{\partial \hat{f}}\right)_1 \\ \cdots & \cdots & \cdots & \cdots & \cdots & \cdots \\ \left(\frac{\partial v}{\partial \hat{a}}\right)_n & \left(\frac{\partial v}{\partial \hat{b}}\right)_n & \left(\frac{\partial v}{\partial \hat{c}}\right)_n & \left(\frac{\partial v}{\partial \hat{d}}\right)_n & \left(\frac{\partial v}{\partial \hat{e}}\right)_n & \left(\frac{\partial v}{\partial \hat{f}}\right)_n \end{bmatrix},$$

$$\hat{x} = \begin{bmatrix} \hat{a} \\ \hat{b} \\ \hat{c} \\ \hat{d} \\ \hat{e} \\ \hat{f} \end{bmatrix},$$

$$L = \begin{bmatrix} 0 \\ \cdots \\ 0 \end{bmatrix}.$$

The least-squares principle, as shown in Eq. (A.4) is also used to fit ellipse, but with the additional constraint condition below (Fitzgibbon et al., 1999).

$$4\hat{a}\hat{c} - \hat{b}^2 = 1 \tag{A.10}$$

In ellipse fitting, we rewrite the above equation as

$$w = 4ac - b^2 - 1, \tag{A.11}$$

where w denotes the residual error for the fitted parameters. This equation can also be linearized as

$$4c \cdot \hat{a} - 2b \cdot \hat{b} + 4a \cdot \hat{c} - 1 + w = 0. \tag{A.12}$$

Alternatively, it can be rewritten in the form below:

$$C\hat{x} + W_x = 0, \tag{A.13}$$

where $\hat{x} = \begin{Bmatrix} \hat{a} \\ \hat{b} \\ \hat{c} \\ \hat{d} \\ \hat{e} \\ \hat{f} \end{Bmatrix}$,

$$C = \begin{bmatrix} 4c & -2b & 4a & 0 & 0 & 0 \end{bmatrix},$$

$$W_x = -1 + w.$$

Thus, Eq. (A.3) and (A.13) are the basic equations for evaluating the errors of each fitted parameter, which can be expressed again as Equation (A.5) but with a different expression for $Q_{\hat{X}\hat{X}}$:

$$Q_{\hat{X}\hat{X}} = N_{BB}^{-1} - N_{BB}^{-1} C^T N_{CC}^{-1} C N_{BB}^{-1}, \tag{A.14}$$

where

$$N_{BB} = B^T B \tag{A.15}$$

and

$$N_{CC} = C N_{BB}^{-1} C^T. \tag{A.16}$$

The errors for the center location, the orientation of the major axis, and the lengths of minor and major axes of the fitted ellipse can be derived from $\hat{x}$ according to the relationships between them and these coefficients using the law of error propagation.

Supplementary materials

Supplementary material associated with this article can be found, in the online version, at doi:10.1016/j.icarus.2018.04.006.

References

Asphaug, E., Melosh, H.J., 1993. The Stickney impact of Phobos: a dynamical model. Icarus 101, 144–164.

Barlow, N.G., 1988. Crater size-frequency distributions and a revised Martian relative chronology. Icarus 75, 285–305.

Barlow, N.G., 2003. Revision of the " Catalog of Large Martian Impact Craters". Abstract 3073, presented at Sixth International Conference on Mars, Calif. Inst. of Technol., Pasadena, Calif., 20– 25 July.

Barnouin, O.S., Zuber, M.T., Smith, D.E., Neumann, G.A., Herrick, R.R., Chappelow, J.E., Murchie, S.L., Prockter, L.M., 2012. The morphology of craters on Mercury: results from MESSENGER flybys. Icarus 219, 414–427.

Besse, S., Lamy, P., Jorda, L., Marchi, S., Barbieri, C., 2012. Identification and physical properties of craters on asteroid (2867) Steins. Icarus 221, 1119–1129.

Binzel, R.P., Gaffey, M.J., Thomas, P.C., Zellner, B.H., Storrs, A.D., Wells, E.N., 1997. Geologic mapping of Vesta from 1994 Hubble Space Telescope images. Icarus 128, 95–103.

Binzel, R.P., Xu, S., 1993. Chips off of asteroid 4 Vesta: evidence for the parent body of achondrite meteorites. Science 260, 186–191.

Bottke, W.F., Love, S.G., Tytell, D., Glotch, T., 2000. Interpreting the elliptical crater populations on mars, venus, and the moon. Icarus 145, 108–121.

Bourke, M.C., Balme, M., Beyer, R.A., Williams, K.K., Zimbelman, J., 2006. A comparison of methods used to estimate the height of sand dunes on Mars. Geomorphology 81, 440–452.

Carr, M.H., et al., 1994. The geology of gaspra. Icarus 107, 61–71.

Crater Analysis Techniques Working Group, 1979. Standard techniques for presentation and analysis of crater size-frequency data. Icarus 37, 467–474.

Cintala, M.J., Mouginis-Mark, P.J., 1980. Martian fresh crater depths: More evidence for subsurface volatiles? Geophys. Res. Lett. 7, 329–332.

Degewij, J., Tedesco, E.F., Zellner, B., 1979. Albedo and color contrasts on asteroid surfaces. Icarus 40, 364–374.

Elbeshausen, D., Wünnemann, K., Collins, G.S., 2013. The transition from circular to elliptical impact craters. J. Geophys. Res. 118, 2295–2309.

Fassett, C.I., Kadish, S.J., Head, J.W., Solomon, S.C., Strom, R.G., 2011. The global population of large craters on Mercury and comparison with the Moon. Geophys. Res. Lett. 38, L10202.

Fitzgibbon, A., Pilu, M., Fisher, R.B., 1999. Direct least square fitting of ellipses. IEEE Trans. Pattern Anal. Mach. Intell. 21, 476–480.

Gaffey, M.J., 1997. Surface lithologic heterogeneity of Asteroid 4 Vesta. Icarus 127, 130–157.

Gou, S., Yue, Z., Di, K., Liu, Z., 2018. A global catalogue of Ceres impact craters ≥ 1 km and preliminary analysis. Icarus 302, 296–307.

Greenberg, R., Bottke, W., Nolan, M., Geissler, P., Petit, J-M., Durda, D., Asphaug, E., Head, J., 1996. Collisional and dynamical history of Ida. Icarus 120, 106–118.

Herrick, R.R., Hessen, K.K., 2006. The planforms of low-angle impact craters in the northern hemisphere of Mars. Meteorit. Planet. Sci. 41, 1483–1495.

Hirata, N., Barnouin-Jha, O.S., Honda, C., Nakamura, R., Miyamoto, H., Sasaki, S., Demura, H., Nakamura, A.M., Michikami, T., Gaskell, R.W., Saito, J., 2009. A survey of possible impact structures on 25143 Itokawa. Icarus 200, 486–502.

Irwin III, R.P., Tanaka, K.L., Robbins, S.J., 2013. Distribution of early, middle, and late Noachian cratered surfaces in the Martian highlands: Implications for resurfacing events and processes. J. Geophys. Res. 118, 278–291.

Ivanov, B.A., Melosh, H.J., 2013. Two-dimensional numerical modeling of the Rheasilvia impact formation. J. Geophys. Res. 118, 1545–1557.

Jaumann, R., 2012. Vesta's shape and morphology. Science 336, 687–690.

Jaumann, R., Nass, A., Otto, K., Krohn, K., Stephan, K., McCord, T.B., Williams, D.A., Raymond, C.A., Blewett, D.T., Hiesinger, H., Yingst, T.A., De Sanctis, M.C., Palomba, E., Roatsch, T., Matz, K.-D., Preusker, F., Scholten, F., Russell, C.T., 2014. The geological nature of dark material on Vesta and implications for the subsurface structure. Icarus 240, 3–19.

Kinser, R.M., Gibbs, V.B., Barlow, N.G., 2013. A New database of craters 5-km-diameter and larger for the Moon: Western nearside. 44th Lunar and Planetary Science Conference, Abstract, 1679.pdf.

Kneissl, T., van Gasselt, S., Neukum, G., 2011. Map-projection-independent crater size-frequency determination in GIS environments—new software tool for ArcGIS. Planet. Space Sci. 59 (11–12), 1243–1254.

Li, J.-Y., McFadden, L.A., Thomas, P.C., Mutchler, M.J., Parker, J.W., Young, E.F., Russell, C.T., Sykes, M.V., Schmidt, B.E., 2010. Photometric mapping of Asteroid (4) Vesta's southern hemisphere with Hubble Space Telescope. Icarus 208, 238–251.

Marchi, S., Bottke, W.F., O'Brien, D.P., Schenk, P., Mottola, S., De Sanctis, M.C., Kring, D.A., Willams, D.A., Raymond, C.A., Russell, C.T., 2014. Small crater populations on Vesta. Planet. Space Sci. 103, 96–103.

Marchi, S., McSween, H.Y., O'Brien, D.P., Schenk, P., De Sanctis, M.C., Gaskell, R., Jaumann, R., Mottola, S., Preusker, F., Raymond, C.A., Roatsch, T., Russell, C.T., 2012. The violent collisional history of Asteroid 4 Vesta. Science 336, 690–694.

McCord, T.B., Adams, J.B., Johnson, T.V., 1970. Asteroid Vesta: spectral reflectivity and compositional implications. Science 168, 1445–1447.

McCord, T.B., 2012. Dark material on Vesta from the infall of carbonaceous volatile-rich material. Nature 491, 83–86.

Melosh, H.J., 1989. Impact Cratering: A Geologic Process. Oxford University Press, New York.

Nathues, A., Hoffmann, M., Schäfer, M., Thangjam, G., Le Corre, L., Reddy, V., Christensen, U., Mengel, K., Sierks, H., Vincent, J-B., Cloutis, E.A., Russell, C.T., Schäfer, T., Gutierrez-Marques, P., Hall, I., Ripken, J., Büttner, I., 2015. Exogenic olivine on Vesta from Dawn Framing camera color data. Icarus 258, 467–482.

O'Brien, D.P., Sykes, M.V., Tricarico, P., 2011. Collision probabilities and impact velocity distributions for Vesta and Ceres. 42nd Lunar and Planetary Science Conference, Abstract, 2665.pdf.

Pike, R.J., 1974. Depth/diameter relations of fresh lunar craters: revision from spacecraft data. Geophys. Res. Lett. 1, 291–294.

Pike, R.J., 1977a. Size-dependence in the shape of fresh impact craters on the moon. In: Roddy, D.J., Pepin, R.O., Merrill, R.B. (Eds.), Impact and Explosion Cratering. Pergamon Press, New York, pp. 489–509.

Pike, R.J., 1980. Formation of complex impact craters: evidence from Mars and other planets. Icarus 43, 1–19.

Pike, R.J., Wilhelms, D.E., 1978. Secondary-impact craters on the Moon: topographic form and geologic process. Lunar Planet. Inst. Sci. IX, 907–909 (abstract).

Platz, T., Michael, G., Tanaka, K.L., Skinner Jr., J.A., Fortezzo, C.M., 2013. Crater-based dating of geological units on Mars: methods and application for the new global geological map. Icarus 225, 806–827.

Polanskey, C.A., Joy, S.P., Raymond, C.A., 2011. Dawn science planning, operations and archiving. Space Sci. Rev. 163, 511–543.

Preusker, F., Scholten, F., Matz, K.-D., Roatsch, T., Jaumann, R., Raymond, C.A., Russell, C.T., 2014. Global shape of Vesta from Dawn FC stereo images. Lunar Planetary Science Conference, Abstract, 2027.pdf.

Rayman, M.D., Fraschetti, T.C., Raymond, C.A., Russell, C.T., 2006. Dawn: a mission in development for exploration of main belt asteroids Vesta and Ceres. Acta Astronaut. 58, 605–616.

Rayman, M.D., Mase, R.A., 2014. Dawn's exploration of Vesta. Acta Astronaut. 94, 159–167.

Richardson, J.E., Melosh, H.J., Greenberg, R.J., O'Brien, D.P., 2005. The global effects of impact-induced seismic activity on fractured asteroid surface morphology. Icarus 179, 325–349.

Roatsch, Th., Kersten, E., Matz, K.-D., Preusker, F., Scholten, F., Elgner, S., Jaumann, R., Raymond, C.A., Russell, C.T., 2013. High resolution Vesta low altitude mapping orbit atlas derived from Dawn Framing Camera images. Planet. Space Sci. 85, 293–298.

Roatsch, Th., Kersten, E., Matz, K.-D., Preusker, F., Scholten, F., Jaumann, R., Raymond, C.A., Russell, C.T., 2012. High resolution Vesta high altitude mapping orbit atlas derived from Dawn Framing Camera images. Planet. Space Sci. 73, 283–286.

Robbins, S.J., 2016. Developing a global lunar crater database, complete for craters ≥1 km. 47th Lunar and Planetary Science Conference, Abstract No. 1525.pdf.

Robbins, S.J., Antonenko, I., Kirchoff, M.R., Chapman, C.R., Fassett, C.I., Herrick, R.R., Gay, P.L., 2014. The variability of crater identification among expert and community crater analysts. Icarus 234, 109–131.

Robbins, S.J., Hynek, B.M., 2012a. A new global database of Mars impact craters ≥1 km: 1. Database creation, properties, and parameters. J. Geophys. Res. 117, E05004.

Robbins, S.J., Hynek, B.M., 2012b. A new global database of Mars impact craters ≥1 km: 2. Global crater properties and regional variations of the simple-to-complex transition diameter. J. Geophys. Res. 117, E06001.

Robinson, M.S., Thomas, P.C., Veverka, J., Murchie, S.L., Wilcox, B.B., 2002. The geology of 433 Eros. Meteorit. Planet. Sci. 37, 1651–1684.

Ruesch, O., Hiesinger, H., Blewett, D.T., Williams, D.A., Buczkowski, D., Scully, J., Yingst, R.A., Roatsch, T., Preusker, F., Jaumann, R., Russell, C.T., Raymond, C.A., 2014. Geologic map of the northern hemisphere of Vesta based on Dawn Framing Camera (FC) images. Icarus 244, 41–59.

Russell, C.T., et al., 2012. Dawn at Vesta: testing the protoplanetary paradigm. Science 336 (6082), 684–686.

Russell, C.T., Coradini, A., Christensen, U., De Sanctis, M.C., Feldman, W.C., Jaumann, R., Keller, H.U., Konopliv, A.S., McCord, T.B., McFadden, L.A., McSween, H.Y., Mottola, S., Neukum, G., Pieters, C.M., Prettyman, T.H., Raymond, C.A., Smith, D.E., Sykes, M.V., Williams, B.G., Wise, J., Zuber, M.T., 2004. Dawn: a journey in space and time. Planet. Space Sci. 52, 465–489.

Russell, C.T., Raymond, C.A., 2011. The Dawn mission to Vesta and Ceres. Space Sci. Rev. 163 (1), 3–23.

Salamunićcar, G., Lončarić, S., Pina, P., Bandeira, L., Saraiva, J., 2011. MA130301GT catalogue of Martian impact craters and advanced evaluation of crater detection algorithms using diverse topography and image datasets. Planet. Space Sci. 59, 111–131.

Salamunićcar, G., Lončarić, S., 2008. Open framework for objective evaluation of crater detection algorithms with first test-field subsystem based on MOLA data. Advances in Space Research 42 (1), 6–19.

Schröder, S.E., Maue, T., Gutiérrez Marqués, P., Mottola, S., Aye, K.M., Sierks, H., Nathues, A., 2013. In-flight calibration of the Dawn Framing Camera. Icarus 226, 1304–1317.

Schröder, S.E., Mottola, S., Matz, K.-D., Roatsch, T., 2014. In-flight calibration of the Dawn Framing Camera II: flat fields and stray light correction. Icarus 234, 99–108.

Shingareva, T.V., Basilevsky, A.T., Shashkina, V.P., Neukum, G., Werner, S., Jaumann, R., Giese, B., Gwinner, K., 2008. Morphological characteristics of the Phobos craters and grooves. 39th Lunar Planetary Science Conference, Abstract, 2425.pdf.

Shoemaker, E.M., Hackman, R.J., Eggleton, R.E., 1962. Interplanetary correlation of geologic time. Adv. Astronaut. Sci. 8, 70–89.
Sullivan, R., Greeley, R., Pappalardo, R., Asphaug, E., Moore, J.M., Morrison, D., Belton, M.J.S., Carr, M., Chapman, C.R., Geissler, P., Greenberg, R., Granahan, J., Head III, J.W., Kirk, R., McEwen, A., Lee, P., Thomas, P.C., Veverka, J., 1996. Geology of 243 Ida. Icarus 120, 119–139.
Tanaka, K.L., Robbins, S.J., Fortezzo, C.M., Skinner, J.A., Hare, T.M., 2014. The digital global geologic map of Mars: chronostratigraphic ages, topographic and crater morphologic characteristics, and updated resurfacing history. Planet. Space Sci. 95, 11–24.
Thomas, P.C., Veverka, J., Bell, J.F., Clark, B.E., Robinson, M., McFadden, L.A., Malin, M.C., Chapman, C.R., Merline, W., Murchie, S., 1999. Mathilde: size, shape, and geology. Icarus 140, 17–27.
Trask, N.J., 1966. Size and spatial distribution of craters estimated from Ranger photographs. Tech. Rep. 32-800. Ranger VIII and IX. Part II – Experimenters' Analses and Interpretations. Pasadena, CA: Jet Propul. Lab.
Turtle, E.P., Pierazzo, E., Collins, G.S., Osinski, G.R., Melosh, H.J., Morgan, J.V., Reimold, W.U., 2005. Impact structures: What does crater diameter mean? Geol. Soc. Am. Spec. Pap. 384, 1–24.
Vincent, J.-B., Besse, S., Marchi, S., Sierks, H., Massironi, M.the OSIRIS team, 2012b. Physical properties of craters on asteroid (21) Lutetia. Planet. Space Sci. 66, 79–86.
Vincent, J.-B., Schenk, P., Nathues, A., 2014. Crater depth-to-diameter distribution and surface properties of (4) Vesta. Planet. Space Sci. 103, 57–65.
Wang, J., Cheng, W., Zhou, C., 2015. A Chang'E-1 global catalog of lunar impact craters. Planet. Space Sci. 112, 42–45.
Williams , D.A., 2014. The geology of the Marcia quadrangle of asteroid Vesta: assessing the effects of large, young craters. Icarus 244, 74–88.
Wood, C.A., Anderson, L., 1978. New morphometric data for fresh lunar craters, Lunar Planet. Sci. Conf. Proc. 9, 3669–3689.
Yingst, A., Mest, S.C., Berman, D.C., Garry, W.B., Williams, D.A., Buczkowski, D., Jaumann, R., Pieters, C.M., DeSanctis, M.C., Frigeri, A., LeCorre, L., Preusker, F., Raymond, C.A., Reddy, V., Russell, C.T., Roatsch, T., Schenk, P.M., 2014. Geologic mapping of Vesta. Planet. Space Sci. 103, 2–23.